Dannis M. Brouwer[2]
e-mail: d.m.brouwer@utwente.nl

(Ger) K. G. P. Folkersma

Steven E. Boer

Ronald G. K. M. Aarts

Mechanical Automation and Mechatronics,
Faculty of Engineering Technology,
University of Twente,
Enschede, P.O. Box 217,
7500 AE, The Netherlands

Exact Constraint Design of a Two-Degree of Freedom Flexure-Based Mechanism[1]

We present the exact constraint design of a two degrees of freedom cross-flexure-based stage that combines a large workspace to footprint ratio with high vibration mode frequencies. To maximize unwanted vibration mode frequencies the mechanism is an assembly of optimized parts. To ensure a deterministic behavior the assembled mechanism is made exactly constrained. We analyze the kinematics of the mechanism using three methods; Grüblers criterion, opening the kinematic loops, and with a multibody singular value decomposition method. Nine release-flexures are implemented to obtain an exact constraint design. Measurements of the actuation force and natural frequency show no bifurcation, and load stiffening is minimized, even though there are various errors causing nonlinearity. Misalignment of the exact constraint designs does not lead to large stress, it does however decrease the support stiffness significantly. We conclude that designing an assembled mechanism in an exactly constrained manner leads to predictable stiffnesses and modal frequencies. [DOI: 10.1115/1.4025175]

1 Introduction

In precision manipulation, repeatability [1] and determinism [2,3] play an important role. Determinism means that given inputs result in consistent responses that are not affected by fortuitous disturbances. In vacuum traditional roller or plain bearings to guide motion suffer from increased friction, hysteresis, and wear. In addition these bearings contaminate the vacuum due to the release of particles, and the evaporation of lubricants. Solutions are to use air or magnetic bearings at much increased cost levels, or to use flexure-based mechanisms. Flexure mechanisms [1–15] behave to a large extent deterministic, because they do not suffer from friction, stiction or backlash, and therefore they show a low hysteresis.

However, flexures inherently lose stiffness in supporting directions when deflected, while the actuation stiffness does not change much [15]. This effect in combination with the introduced stress when deflected, limits the range of motion [3,7,13,17]. We have to distinguish two types of stiffnesses. The mechanism motions associated with the actuation stiffness should ideally be low in stiffness because they need to be actuated. The supporting stiffness should ideally be high to result in high natural frequencies associated with the uncontrollable modes. The higher the natural frequencies for these unwanted modes, the less disturbances from the outside like shocks influence the position of the end-effector with respect to the base, and the better the precision. Examples of confined vacuum spaces where high support stiffness and high natural frequencies over a large range of motion are important are found in extreme ultraviolet and E-beam lithography machines, and SEM and TEM microscopes. Other applications can be found in satellites where the mass of a mechanism is of utmost importance.

Figure 1 shows a drawing of the two-DOF flexure-based mechanism. To obtain a large ratio of support stiffness in relation to the actuation stiffness, a lumped compliance design approach has been used [3]. Wiersma [16] has maximized the unwanted frequencies of several hinge designs over a ± 20 deg range of motion with a load representative for the base mounted flexures of this two-DOF mechanism while constraining the allowable stress. It turns out that the optimal leaf-spring geometry of the flexure hinges combines a small thickness and length, such that the maximum stress criterion is met at the maximum deflection. Therefore, for static, dynamic, and also elastic stability reasons the compliance should be concentrated or lumped, resulting in flexure hinges. The cross-flexure hinges are tuned to maximize the lowest natural frequency [17]. The used flexures have relatively large dimensions in the out of plane direction, and have a 3D shape. The design of the arms has been optimized for low mass and high stiffness. Monolithic positioning mechanisms fabricated, for example, wire EDM, water jet, or deep reactive ion etching naturally have less misalignment problems, although temperature gradients could still cause small misalignments. While this is a convenient and precise method of fabricating flexure-based mechanisms, it is difficult to create high stiffness low mass optimized features with a 3D geometry. The proposed mechanism therefore consists of many discrete parts.

To guarantee deterministic behavior with the many assembled parts, the mechanism is designed to be exactly constrained [2,3,18,19]. Exact constraint design, as opposed to elastic averaging, does not require tight tolerances on flatness, parallelism, and squareness, and it allows for temperature fluctuations without excessive stress in the structure. In mechanisms with roller or plain bearings internal loading causes excessive friction and wear. Internal stress caused by a combination of overconstraining and misalignment in flexure-based mechanisms can lead to load stiffening [20] and bifurcation [21]. Load stiffening arises when a planar mechanism, like the two-DOF mechanism, shows overconstraints in a planar analysis. Then overconstraints directly affect the actuation stiffness. Bifurcation arises when the internal stress due to misalignment exceeds the elastic stability limit of flexures. Meijaard et al. [21] have shown that a misalignment angle of several tenths of milliradians can be sufficient to provoke bifurcation in an overconstrained parallel leaf-spring flexure. The bifurcation results in a stiffness reduction of roughly one order in the intended stiff support directions. Lumped compliance overconstrained designs are sensitive for misalignments because they bifurcate at small misalignments. Therefore, the two-DOF mechanism is designed to be exactly constrained.

In a kinematic analysis of DOFs and constraints joints are assumed infinitely stiff in certain directions while being infinitely compliant in others. In reality flexure joints have a relatively high stiffness in certain directions while having a small stiffness in

[1]Some preliminary results were presented in DETC2012-70377 [17].
[2]Corresponding author.

Contributed by the Mechanisms and Robotics Committee of ASME for publication in the Journal of Mechanisms and Robotics. Manuscript received February 8, 2013; final manuscript received July 19, 2013; published online September 11, 2013. Assoc. Editor: Philippe Wenger.

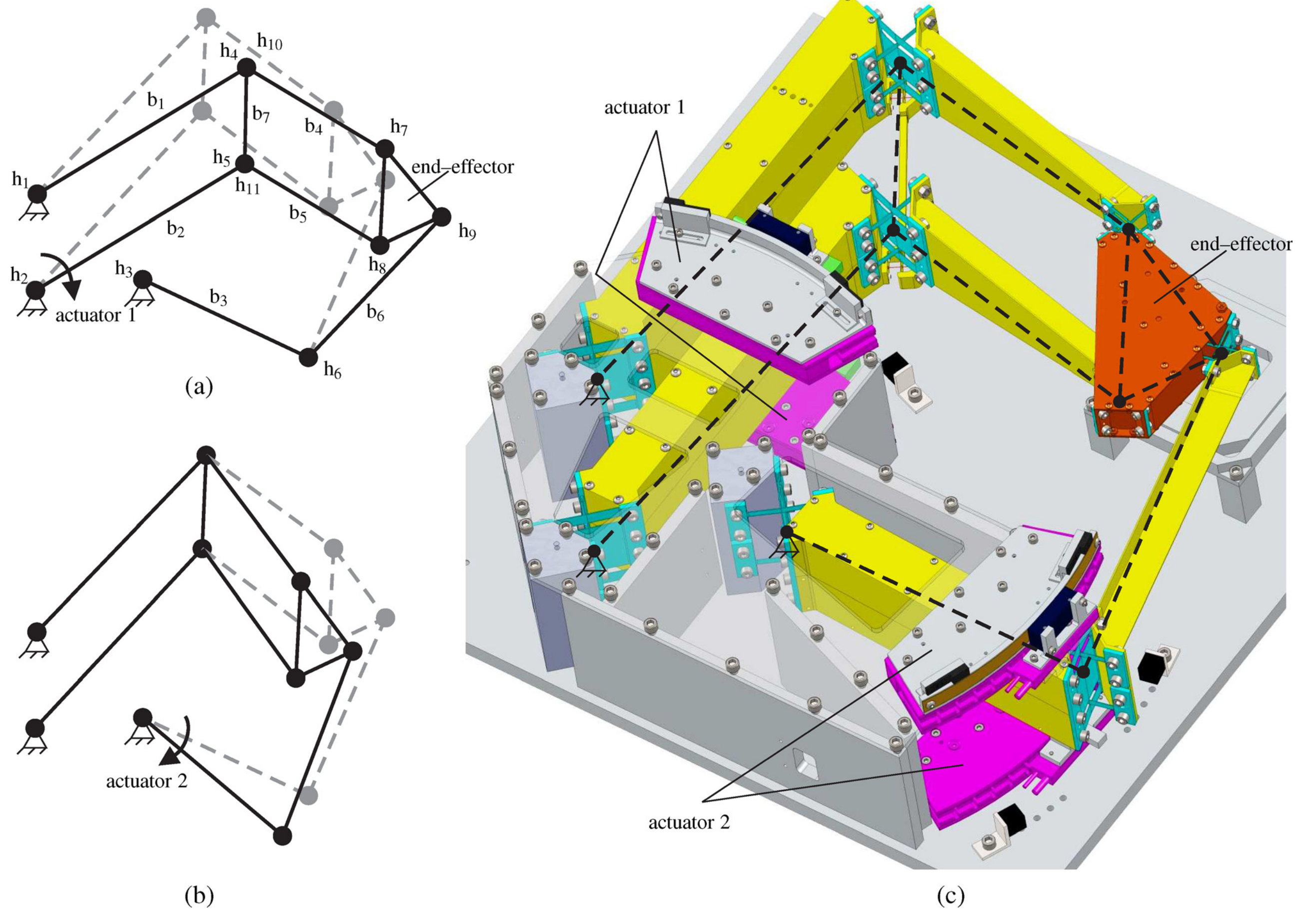

Fig. 1 Two-DOF mechanism allowing for base mounted actuators; (*a*) shows the motion resulting from driving actuator 1 and constraining actuator 2; (*b*) shows the motion resulting from driving actuator 2 and constraining actuator 1; (*c*) shows a drawing of the mechanism with top plate removed

others. The flexure hinges of the two-DOF stage consist of a leaf-spring kinematically in parallel with two perpendicular wire-flexures [17]. A leaf-spring is stiff in three DOFs and a wire-flexure is stiff in one DOF [3]. Together the flexure hinge has five stiff directions with respect to one low rotational stiffness. The rotational stiffness of the used hinges are in fact at least a 1000-times more compliant than the stiffness of the support directions [16,17]. Therefore, kinematically the hinges are treated as ideal hinges, constraining five DOFs and leaving free only the in-plane rotation. The flexure hinges will also cause in-plane displacements when rotated due to the shift of the instant center of rotation. This parasitic motion, however, will not influence the constraint analysis because the parasitic displacements are part of the motion the mechanism facilitates, so they will not lead to self-stress.

To investigate if and where a mechanism is overconstrained several methods can be used. Analysis can be based on counting the DOFs of the free bodies and the number of constraints. Maxwell [22] determined the number of overconstraints in trusses, valid for a general case, by counting the number of bars and subtracting the degrees of freedom of the nodes. Chebychev [23] determined the number of degrees of freedom of the freed bars and the number of constraints imposed by the joints. Grübler [24] proposed a count similar to Maxwell's, but with the inclusion of bars with more than two connections. Kutzbach [25] made a generalization to include spatial mechanisms. A constraint analysis of the two-DOF mechanism using the Grübler criterion will be shown in Sec. 3. In case of a mechanism with overconstraints the Grübler criterion predicts an erroneous mobility. Blanding [18] describes a constraint analysis based on ideal constraints. An ideal constraint is approximated as having infinite compliance perpendicular to the constraint's line of action and infinite stiffness along the constraint's line of action. This model, although simplistic, is adequately descriptive for finding the directions of free motion. However, analyzing the overconstraints requires another approach. A generalized formula calculating the mobility taking into account overconstraints lacks.

A solution is opening each kinematic loop, and analyzing the constraints meeting at the connections. This method will be shown for the two-DOF mechanism in Sec. 4. However, in complex structures the approach might not succeed, because it requires a large level of understanding.

Another solution is to determine the rank of the homogeneous linear set of constraint equations as proposed by Besseling [26], Pellegrino and Calladine [27], Angeles and Gosselin [28], and Aarts et al. [29]. Aarts et al. show that, based on a flexible multibody modeling approach and the singular value decomposition (SVD) of a specific Jacobian matrix, both under- and overconstraints can be determined. Overconstrained modes are visualized by plotting the modes of self-stress in stress distributions of the mechanism. This method will be shown for the two-DOF mechanism in Sec. 5.

In this paper, we will show three methods for analyzing the constraints of the two-DOF mechanism; Grübler's criterion in Sec. 3, opening the kinematic loops in Sec. 4, and using a multibody singular value decomposition method in Sec. 5. These analyses will be preceded by the background of the conceptual design of the two-DOFs stage in Sec. 2. With the overconstrained modes known a choice can be made where to release the overconstraints. In Sec. 6, we will show the locations of the implemented releases in the designed and fabricated two-DOF mechanism. To verify the predictability of the two-DOF stage we compare measurements with modeling results of the actuation stiffness and the vibration mode frequencies in Sec. 7, after which conclusions are drawn.

2 Conceptual Design

The conceptual design of the two-DOF flexure-based mechanism shown in Fig. 1, has been explained more elaborate by Folkersma et al. [17]. A mechanism was selected that allowed base mounting of the two actuators, while four DOFs are constrained. The proposed mechanism is based on a planar parallel kinematic mechanism (PKM) with planar hinges and rigid bars. Figure 1 shows the two mechanism motions. It consists of 11 hinges numbered h_1–h_{11} and seven bars b_1–b_7 and the end-effector b_8. The mechanism consists of two parallelograms h_1–h_{10}–h_{11}–h_2 and h_4–h_7–h_8–h_5 to constrain the in-plane rotation of the end-effector, leaving two remaining in-plane translational DOFs. One DOF is driven by an actuator at hinge b_2, the other DOF is driven by an additional bar pair b_3–b_6 with an actuator at hinge h_3. The use of the additional bar pair allows both of the actuators to be placed at the base of the mechanism, avoiding the need to add the full weight of an actuator to the moving mass.

While this particular layout might have a lower performance in terms of supporting stiffness compared to more symmetrical mechanisms, the footprint is relatively small and the in-plane rotation of the end-effector is constrained passively. Also the hinges connected to the base are located at one side of the mechanism, which allows the end-effector with arms to move away, allowing access to a possible work piece.

The kinematics of the mechanism were optimized for a minimum footprint given a workspace of 100×100 mm, and a constraint on the range of motion of the flexures of 40 deg. For this layout optimization, a parametric kinematic model of the mechanism was made in the multibody simulation program spacar, consisting of rigid bars connected in their pivot points with hinges. We used a modified version of the Nelder-Mead simplex method [30] to minimize the footprint. The size of the complete mechanism is $540 \times 585 \times 87$ mm and the workspace-area to footprint ratio is $\frac{1}{32}$. This is large compared to [13,31–35].

The cross-flexure hinges were tuned and oriented to maximize the lowest unwanted natural frequency.

3 Constraint Analysis Using Grübler's Criterion

The number of DOFs and overconstraints can be analyzed by Grübler's criterion [24].

In a two-dimensional analysis a rigid body has three DOFs; thus when n bars are fully free from one another, the mechanism has $3n$ DOFs. Each hinge requires that a certain point of a bar coincides permanently with a certain point of another. Thus, the two coordinates must be the same for both points. The number of DOFs of the mechanism becomes $3n - 2s$, with s is the number of hinges. But, we are only concerned with the relative motions of the bars and not with the motion (of three DOFs) of the mechanism as a whole. Hence, the mobility M according to Grüblers criterion

$$M = 3n - 2s - 3 \quad (1)$$

Analogues arguments hold for a three-dimensional analysis. Rigid bodies then have six DOFs, the hinges constrain five DOFs, and the mobility according to Grüblers criterion becomes

$$M = 6n - 5s - 6 \quad (2)$$

In a two-dimensional planar analysis of the two-DOF mechanism the nine rigid bars, including the base, with each three DOFs sum up to 27 DOFs. The eleven hinges each constrain two DOFs so there are 22 constraints in total and only five DOFs remain in the system. The three rigid body modes of the mechanism are not considered, and therefore subtracted from the system's DOFs. Then, there are two DOFs more than there are constraints as is summarized in Table 1. Because the mobility is twofold, there are no overconstraints in-plane. With the two actuators the mechanism in-plane is exactly constrained.

The mechanism can also be analyzed including the third dimension by Grübler's criterion. The nine bars now give rise to 54 DOFs, the four hinges impose 55 constraints, and 6 rigid-body modes are not considered. As shown in Table 1 this results in nine more constraints than there are DOFs. Because the two-DOF mechanism has a mobility of two, there have to be nine overconstraints. The overconstraints do not appear in the two-dimensional analysis, but do show up in the three-dimensional analysis. Apparently, the overconstraints are related to the out-of-plane directions. There are nine releases and two actuators required to obtain an exact constraint mechanism.

The Grübler's analysis only results in the correct mobility number if the amount of overconstraints are known. Or the other way around, the correct number of overconstraints only shows when the mobility is known. In addition, the direction of the under- and overconstraints does not result from the analysis.

Table 1 Constraint analysis of a four-bar mechanism using Grübler's criterion

	2D	3D	
DOFs of rigid bars ($n = 9$)	27	54	DOFs
Constraints of hinges ($s = 11$)	−22	−55	DOFs
Rigid body modes of mechanism	−3	−6	DOFs
DOFs-constraints-rigid body modes (M)	2	−7	DOFs
Existing mobility (underconstraints)	2	2	
Overconstraints	0	9	

4 Constraint Analysis Opening the Loops

A second approach to determine the mobility and number of overconstraints of the two-DOF mechanism is by opening the loops of the mechanism. Therefore, the two-DOF stage is split up in two subassemblies.

4.1 Loop 1. Subassembly 1, shown in Fig. 2, shows the constraints and free motions of the two parallel paths analyzed at hinge h_{11}. It is as if the four-bar mechanism b_1–b_7–b_2–base is being assembled, and joint h_{11} is the last connection in the loop to fit together. Again, the analysis is made assuming that each hinge permits exactly 1 rotation, the bars are rigid, and actuator 1 constrains exactly one DOF.

In-plane there are four constraints, x_B, y_B, θ_A, and θ_B. The rotational constraint between θ_A and θ_B is however released by hinge h_{11}. Therefore, the four-bar mechanism is constrained three times

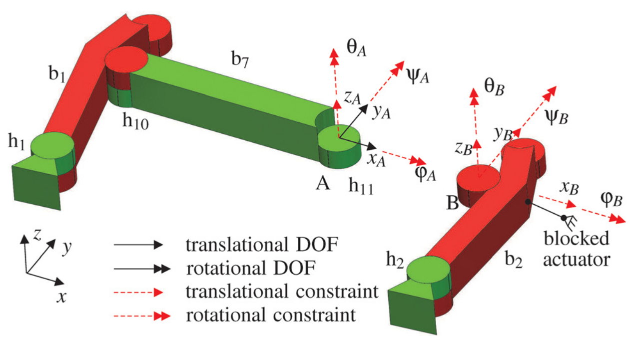

Fig. 2 Constraint analysis by opening loop h_1–b_1–h_{10}–b_7–h_{11}–b_2–h_2–base. The DOFs (solid vectors) and constraints (dashed vectors) are shown for points A and B.

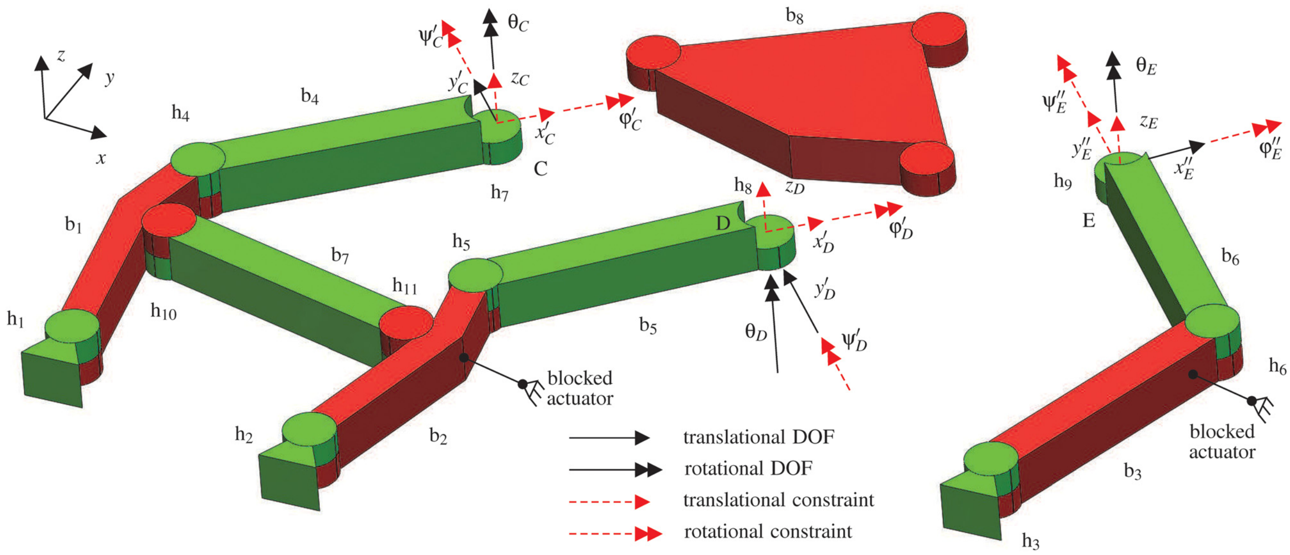

Fig. 3 Analysis of the constraints on end-effector b_8. The DOFs (solid vectors) and constraints (dashed vectors) are shown for points C, D, and E. Actuators 1 and 2 are considered to be constrained. For displaying purposes hinges h_4 and h_{10}, and hinges h_5 and h_{11} are spaced apart, this does not influence the constraint analysis.

in-plane, which makes the mechanism exactly constrained in-plane.

In the out-of-plane direction, however there are six constraints; z_A, φ_A, ψ_A, z_B, φ_B, ψ_B, while three constraints are required for an exactly constrained four bar mechanism. The four bar mechanism is three times overconstrained.

4.2 Loops 2 and 3. Subassembly 2, shown in Fig. 3, can be analyzed by assuming that the actuators are constraining the actuated DOFs. In that case the mechanism of subassembly 1 is constrained and hinges h_4, h_5, and h_6 can be assumed to be attached directly to the base. Subassembly 2 is then simplified to four rigid bars, b_4, b_5, b_6, b_8, and six hinges. Three in-plane DOFs, x'_C, x'_D, and y''_E, are constraining the in-plane mobility of the end-effector, b_8, exactly. However, the out-of-plane mobility which should be constrained three times is constrained nine times by $z'_C, \varphi'_C, \psi'_C, z'_D, \varphi'_D, \psi'_D, z_E, \varphi''_E$, and ψ''_E. Therefore, it can be concluded that subassembly 2 is overconstrained six times.

Subassembly 1 and 2 combined overconstrain the system nine times. All overconstraints are related to the out-of-plane direction, which is not surprising because the mechanism in a two-dimensional analysis is designed as being exactly constrained.

With respect to the Grübler method, the opening-the-loop method provides the correct mobility number without knowing the number of overconstraints beforehand. In addition the method gives the direction of the mobility and overconstraints. However, in complex spatial structures the approach might not succeed, because errors are easily made. A more fail safe mathematical analysis is presented next in Sec. 5.

5 SVD Constraint Analysis Method

In this section, the concept of the multibody analysis using a SVD will be briefly explained. For a more elaborate explanation we refer to Aarts et al. [29].

5.1 Multibody Model Description. A multibody system is used to model the kinematic behavior of interconnected rigid bodies, each of which may undergo large translational and rotational displacements. A set of nodal coordinates $\boldsymbol{x}^{(k)}$ describes the locations and orientations of the nodes of an element k relative to a fixed coordinate system. A set of deformation coordinates $\boldsymbol{\varepsilon}^{(k)}$ describes the element deformation modes. The deformation coordinates are explicitly described as nonlinear deformation functions of the nodal coordinates

$$\boldsymbol{\varepsilon}^{(k)} = \mathcal{D}^{(k)}\boldsymbol{x}^{(k)} \tag{3}$$

The entire multibody system can be assembled of finite elements by defining a global vector $\boldsymbol{x}$ of all nodal coordinates. The deformation functions of the elements can be collected in a global vector $\boldsymbol{\varepsilon}$ for which we can write the nonlinear vector function

$$\boldsymbol{\varepsilon} = \mathcal{D}(\boldsymbol{x}) \tag{4}$$

The vectors $\boldsymbol{x}$ and $\boldsymbol{\varepsilon}$ can be partitioned in invariant nodal coordinates and deformations having a fixed prescribed value $\boldsymbol{x}^{(\mathrm{o})}$ and $\boldsymbol{\varepsilon}^{(\mathrm{o})}$, dependent nodal coordinates or deformations $\boldsymbol{x}^{(\mathrm{c})}$ and $\boldsymbol{\varepsilon}^{(\mathrm{c})}$, and independent (or generalized) nodal coordinates or deformations $\boldsymbol{x}^{(\mathrm{m})}$ and $\boldsymbol{\varepsilon}^{(\mathrm{m})}$. The number of independent nodal coordinates or deformations $n_x^{(\mathrm{m})} + n_\varepsilon^{(\mathrm{m})} = n_{\mathrm{indof}}$ is the number of intended DOFs.

Constraint conditions are applied to restrict the kinematical degrees of freedom of one body in relation to another. The combined system of nonlinear constraint equations should be solvable for the unknown dependent nodal coordinates $\boldsymbol{x}^{(\mathrm{c})}$ as a function of the invariant deformation coordinates $\boldsymbol{\varepsilon}^{(\mathrm{o})}$ and the independent deformation coordinates $\boldsymbol{\varepsilon}^{(\mathrm{m})}$. These are related in matrix $\boldsymbol{J}$, the partial differentiation of the invariant and the independent deformation functions with respect to the dependent nodal coordinates.

$$J = \begin{bmatrix} \dfrac{\partial \boldsymbol{\varepsilon}^{(\mathrm{o})}}{\partial \boldsymbol{x}^{(\mathrm{c})}} \\[2ex] \dfrac{\partial \boldsymbol{\varepsilon}^{(\mathrm{m})}}{\partial \boldsymbol{x}^{(\mathrm{c})}} \end{bmatrix} \tag{5}$$

To solve the system, the number of unintended DOFs n_{undof} and overconstraints n_{oc} should be zero. Then, the matrix $\boldsymbol{J}$ is square and regular, and the dependent velocities can be calculated from the independent velocities. With n_x the total number of nodal coordinates, $n_x^{(\mathrm{o})}$ and $n_\varepsilon^{(\mathrm{o})}$ the number of constrained nodal coordinates and deformation mode coordinates becomes [19]

$$n_{\mathrm{indof}} + n_{\mathrm{undof}} = n_x - (n_x^{(\mathrm{o})} + n_\varepsilon^{(\mathrm{o})}) + n_{\mathrm{oc}} \tag{6}$$

Table 2 Constraint analysis multibody coordinate counting

	11 nodal locations 6 DOF each	66	
	11 hinges 1 DOF each	11	
n_x			77
n_x^o	3 fixed nodal locations		18
n_x^m			0
n_x^c			59
	b_3, b_4, b_5, b_6, and b_7 with 6 constrained modes	30	
	b_1, b_2, and b_8 with 12 constrained modes	36	
n_ε^o			66
n_ε^m	2 actuated hinges		2
$n_{oc} - n_{undof}$	$(n_x^m + n_\varepsilon^m + n_x^o + n_\varepsilon^o - n_x)$		9

Using Eq. (6), the overconstraints of the two-DOF mechanism can be analyzed. There are 11 nodal locations with 6 nodal coordinates each, shown in Fig. 1, and there are eleven hinges which introduce another 11 nodal coordinates, see Table 2. So in total n_x is 77. There are 18 fixed nodal coordinates resulting from the three nodal locations fixed to the base. The total number of dependent nodal coordinates, which need to be calculated, is then 59. Beams b_3, b_4, b_5, b_6, and b_7 have 6 constrained modes each, fixing the two nodal locations in respect to each other. Body b_1, b_2, and b_8 have 12 constrained modes each, fixing the three nodal locations attached to the body in respect to each other. So there are 66 constrained deformation mode coordinates. Then, according to Eq. (6) $n_{oc} - n_{undof} = 7$. It means there are 7 more overconstraints than there are unwanted DOFs. Essentially, this is the same result as Grübler's criterion gave in Table 1. However, two hinges have independent deformation coordinates, because they are actuated, so $n_{oc} - n_{undof} = 9$. Again, the multibody coordinate counting and the Grübler's analysis only result in the correct number of overconstraints or mobility if one of the two is known. If n_{oc} is equal to n_{undof} and unequal to zero, matrix $\boldsymbol{J}$ is square. Only counting multibody coordinates gives the false impression that the system is exactly constrained. Therefore, matrix $\boldsymbol{J}$ must also be nonsingular, or equivalently the matrix $\boldsymbol{J}$ should have full rank.

5.2 SVD Method. For any square or rectangular matrix the rank can be determined from its SVD which for $\boldsymbol{J}$ can be written as

$$\boldsymbol{J} = \boldsymbol{U}\Sigma\boldsymbol{V}^T \tag{7}$$

where Σ is an $m \times n$ diagonal matrix with non-negative real numbers on the diagonal known as the singular values of $\boldsymbol{J}$, m denoting the number of rows in $\boldsymbol{J}$, and n is the number of columns. $\boldsymbol{U}$ is an orthogonal $m \times m$ matrix, and $\boldsymbol{V}$ is an orthogonal $n \times n$ matrix. A mechanism is exact constraint if the matrix $\boldsymbol{J}$ has full rank. Matrix $\boldsymbol{J}$ has full rank if its inverse exists, which means matrix $\boldsymbol{J}$ is square, i.e., $m = n$, and all singular values are positive.

We consider the nodal forces $\boldsymbol{f}$ and the vector of generalized stress resultants $\boldsymbol{\sigma}$ in the elements. These forces and stress resultants are dual to the velocities $\dot{\mathbf{x}}$ and $\dot{\boldsymbol{\varepsilon}}$, respectively. Each column in $\boldsymbol{U}$ accompanying one of the zero singular values or an excess row of $\boldsymbol{J}$ gives a nonzero solution of the generalized stress resultants $\boldsymbol{\sigma}^{(o)}$ and $\boldsymbol{\sigma}^{(m)}$ that represent a set of statically indeterminate stresses (overconstraints) [29]. A visualization of the stress distribution is proposed by Boer et al. [36]. The matrix $\boldsymbol{U}$ has been processed to give a distribution of the von Mises stress, bending stress or shear stress component. These stresses are combined into an equivalent von Mises stress. The absolute value of the stress has no meaning as it can be scaled. The distribution shows the locations where stress can be expected due to an overconstraint. The stress in reality will be zero if the alignment of the parts is perfect. With increased misalignment the stress level will increase proportionally.

For completeness we state that each column in $\boldsymbol{V}$ accompanying one of the zero singular values or excess columns specifies a vector of velocities which represents the motion of a kinematically indeterminate mode [29] (an underconstrained mode, which is equal to the motion associated with the mobility if no independent coordinates have been chosen).

5.3 Loop 1. The overconstraints of the four-bar mechanism of Fig. 2 can be analyzed using the SVD method with visualization, shown by Brouwer [19]. The hinges release only the rotation in the θ direction, and constrain all other five DOFs. Loop h_1–b_1–h_{10}–b_7–h_{11}–b_2–h_2–base will be analyzed. Figure 4 shows the von Mises stress distribution in this first loop due to the three overconstraints, which can be compared with the overconstraints shown in Fig. 2. Figure 4(*a*) shows a stress distribution mainly due to torsion in beam b_1 and bending primarily in beams b_2 and b_7.

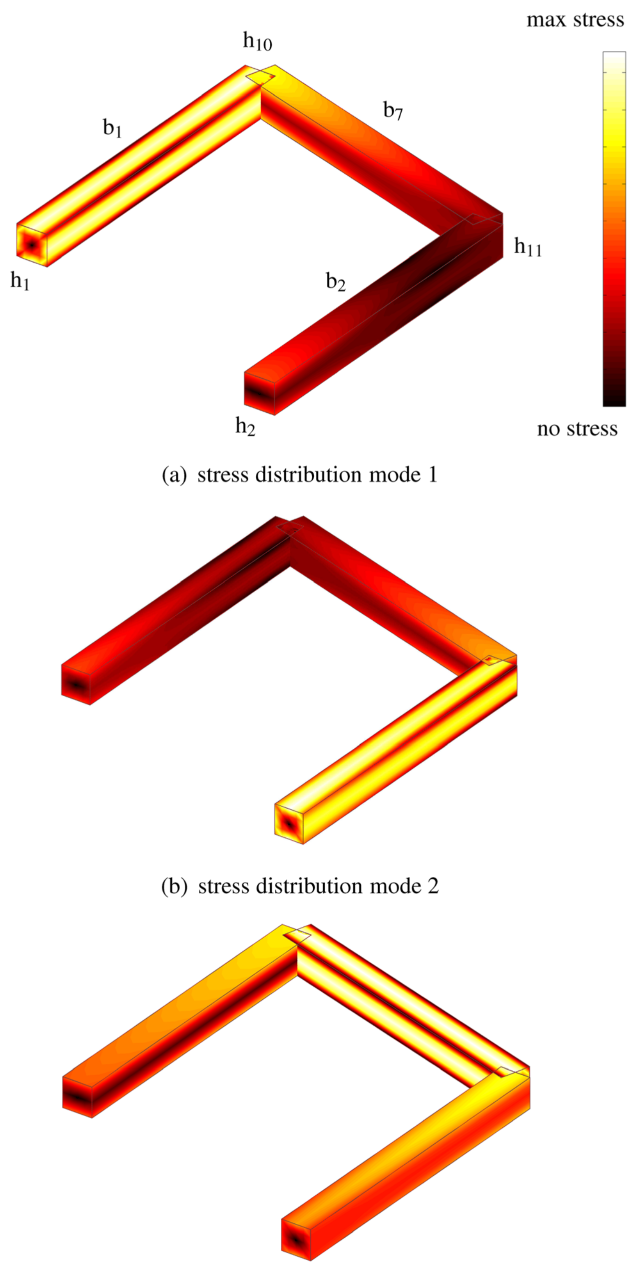

(a) stress distribution mode 1

(b) stress distribution mode 2

(c) stress distribution mode 3

Fig. 4 The three von Mises stress distributions resulting from the three overconstraints in loop h_1–b_1–h_{10}–b_7–h_{11}–b_2–h_2–base

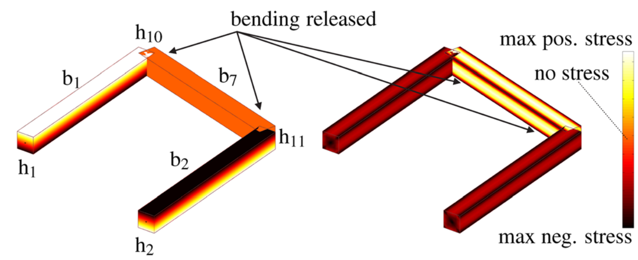

Fig. 5 The stress distribution in loop h_1–b_1–h_{10}–b_7–h_{11}–b_2–h_2–base with bending released at both ends of bar b_7; (*a*) the bending stress component. (*b*) The shear stress component. Please note that the von Mises stress scale differs from the bending and shear stress scale.

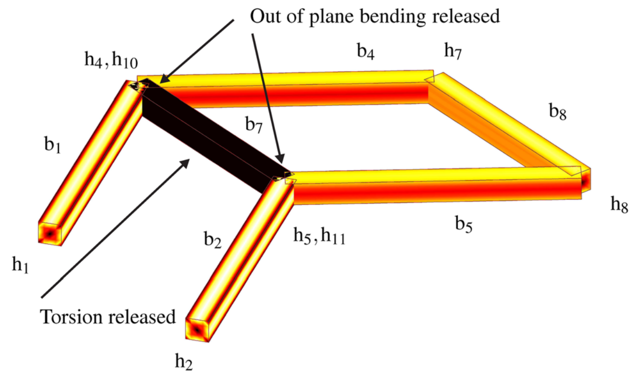

(a) stress distribution mode 1

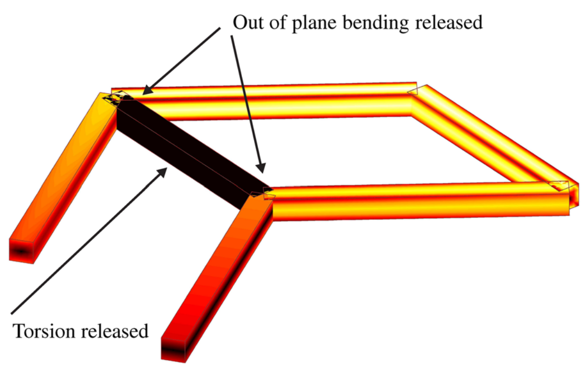

(b) stress distribution mode 2

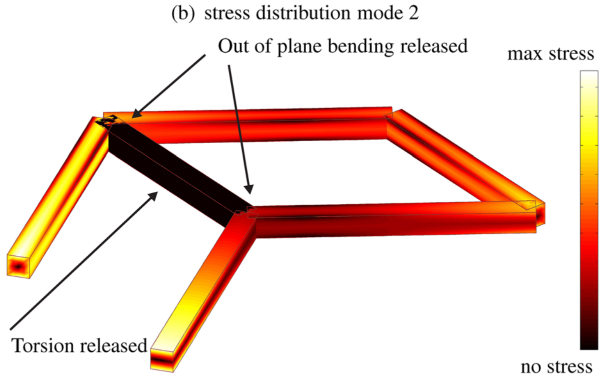

(c) stress distribution mode 3

Fig. 6 The von Mises stress distributions due to the three overconstraints due to the addition of h_4–b_4–h_7–b_8–h_8–b_5–h_5 on the exact constrained loop h_1–b_1–h_{10}–b_7–h_{11}–b_2–h_2–base

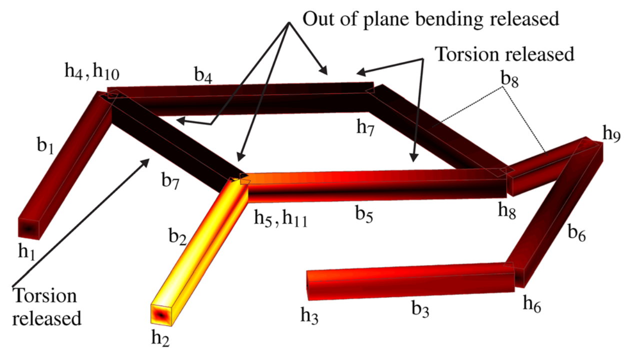

(a) stress distribution mode 1

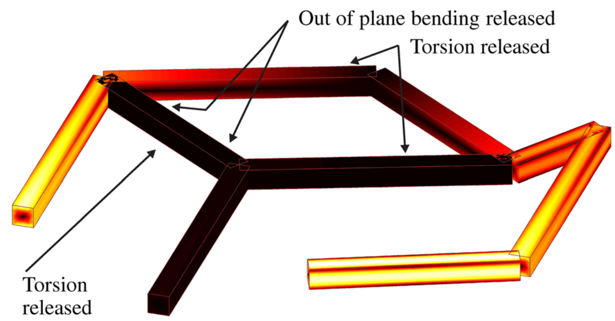

(b) stress distribution mode 2

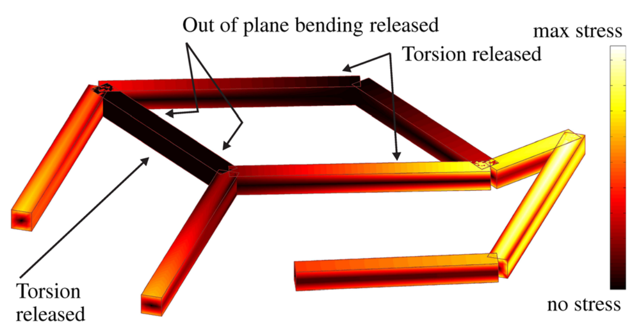

(c) stress distribution mode 3

Fig. 7 The von Mises stress distributions due to the three overconstraints due to the addition of h_3–b_3–h_6–b_6–h_9 on the end-effector b_8

Figure 4(*b*) shows a stress distribution mainly due to a torsional overconstraint in beam b_2 and bending primarily in beams b_1 and b_7. Figure 4(*c*) shows a stress distribution mainly due to a torsional overconstraint in beam b_7 and bending primarily in beams b_1 and b_2. So, the SVD analysis shows in accordance to the "opening the loops" analysis that there are three overconstraints with three overconstrained stress distributions. The distribution in Fig. 4(*a*) is closely related to the double constrained z_A and z_B in Fig. 2. The distribution in Fig. 4(*b*) is closely related to the double constrained ψ_A and ψ_B in Fig. 2. The distribution in Fig. 4(*c*) is closely related to the double constrained φ_A and φ_B in Fig. 2.

Using the SVD method it can be checked at which locations releases can be inserted to reduce the overconstraints. This can be done by implementing releases one by one. We jump to two inserted releases in ψ direction at both ends of beam b_7. The four-bar mechanism then has only one overconstrained stress mode left, which is shown in Fig. 5. Both releases contribute to lowering the number of overconstraints. One extra release is required to

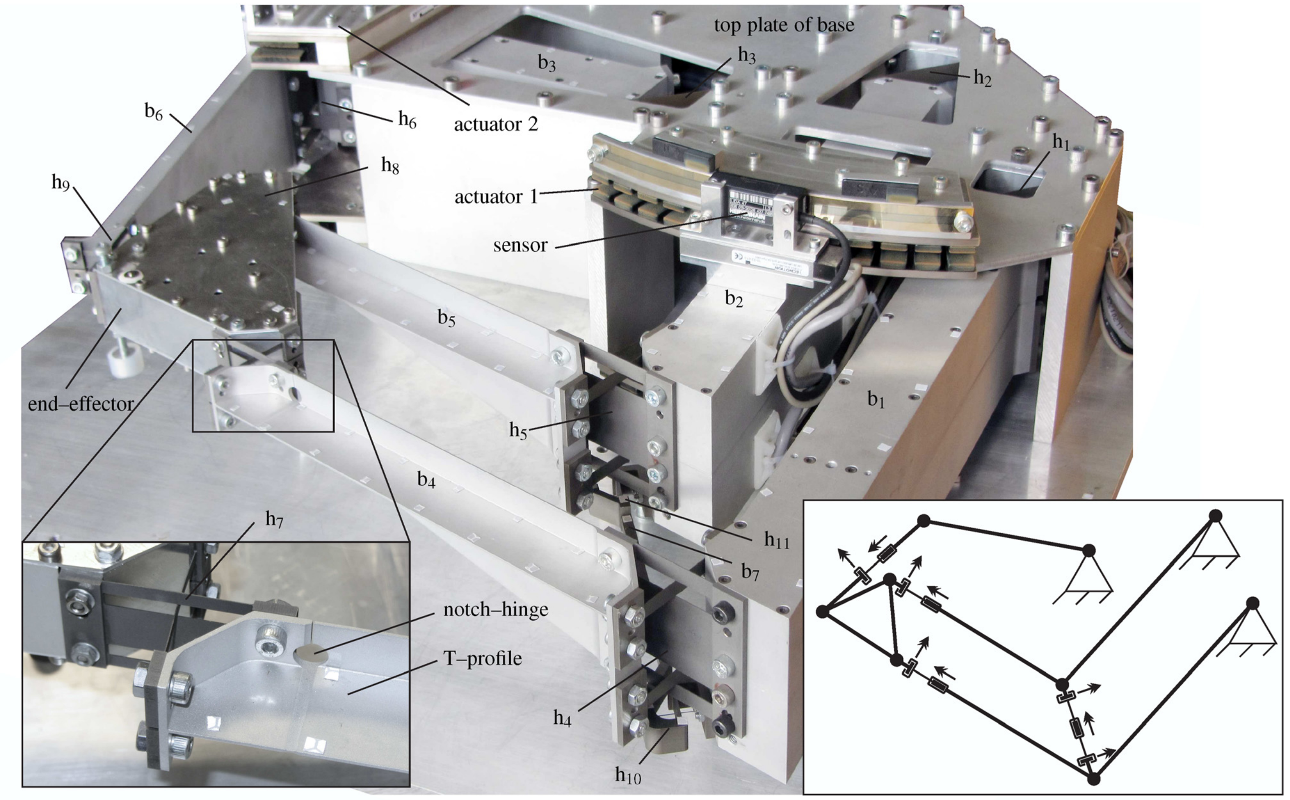

Fig. 8 Photo of the two-DOF mechanism with skeleton frame showing the nine release locations and orientations, double arrows indicating rotational DOFs

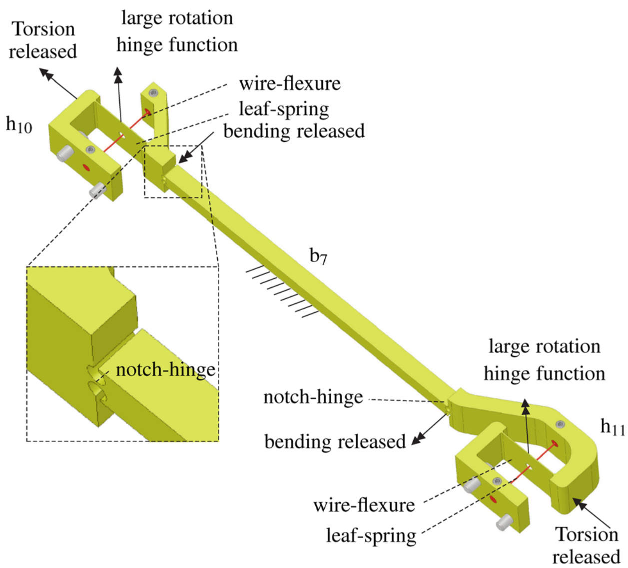

Fig. 9 DOFs of bar b_7

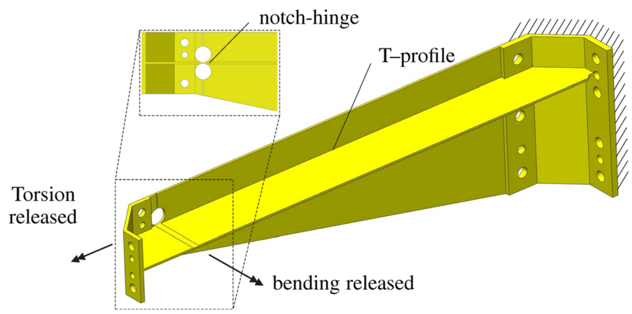

Fig. 10 Torsionally and bending compliant arm

obtain an exact constraint mechanism. The stress distribution shows that beams b_1 and b_2 are loaded mainly by bending and beam b_7 is loaded purely by torsion. To release the third overconstraint of the four-bar mechanism, either bending in φ-direction should be released somewhere in beam b_1 or b_2, or torsion should be released in beam b_7. In Ref. [19], it is shown that for maximizing the stiffness at the end-effector, the path of beams directly toward this end-effector should preferably not contain releases. Because beams b_1 and b_2 are in the stiff path toward the end-effector, we chose to implement the releases in beam b_7. Therefore, we chose to release torsion in beam b_7, and we implicitly chose to insert the first two releases also in beam b_7. It can also be concluded that all the stress modes in loop 1 show out-of-plane stress. This was expected because the mechanism is exactly constrained in-plane.

5.4 Loop 2. With the three inserted releases in loop 1, loop 2, h_4–b_4–h_7–b_8–h_8–b_5–h_5, is added and analyzed. In the model, the hinges h_4 and h_5 coincide with hinges h_{10} and h_{11}. For the constraint analysis this has no influence. Figure 6 shows three overconstrained modes, which again are all related to the out-of-plane direction. As shown in Secs. 4 and 5.3, the result of adding a four-bar mechanism is three out-of-plane overconstraints. There is no von Mises stress in beam b_7, because is has three releases.

In Ref. [19], it is shown that for maximizing the stiffness at the end-effector, releases in the stiff path of beams toward the end-effector, should be placed close to the end-effector. Therefore, a bending release is inserted in beam b_4 near hinge h_7. Torsion has been released in beams b_4 and b_5.

5.5 Loop 3. Having made loops 1 and 2 exactly constrained, the arm, h_3–b_3–h_6–b_6–h_9, is added. This creates another loop, with yet three overconstraints. The SVD analysis, shown in Fig. 7,

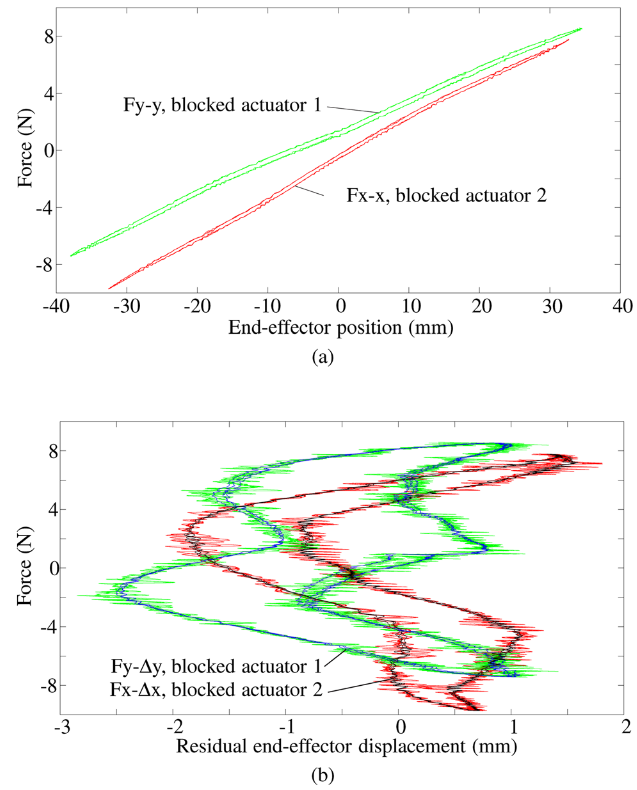

Fig. 11 (*a*) Force-position measurement with one of the actuators blocked, (*b*) unfiltered and filtered force-residual displacement measurement with one of the actuators blocked

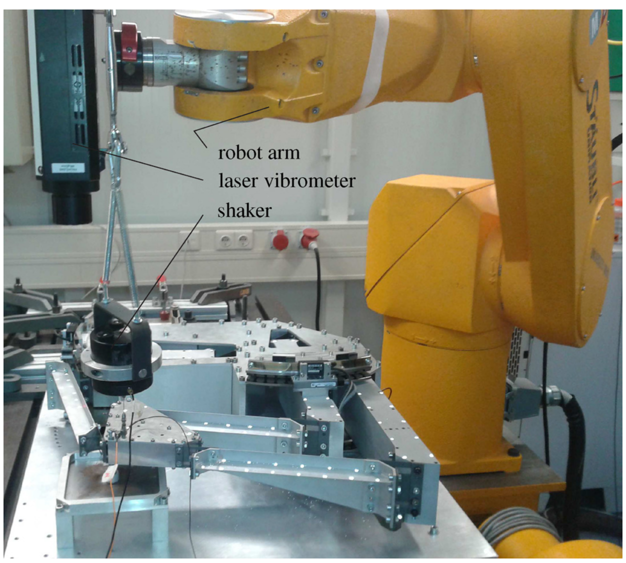

Fig. 12 Beams h_7 and h_{10} showed misalignment after several experiments

indeed shows three modes. The bending and torsion stress in beam b_7 is zero, the torsion stress in beams b_4 and b_5 is zero, and the bending stress in b_4 near h_7 is zero. Clearly, the stress in b_3 and b_6 is high in all cases. To make the entire mechanism exactly constrained bending releases are inserted in beam b_5 near hinge h_8, and in beam b_6 near hinge h_9, and torsion is released in beam b_6.

6 Inserting the Releases

To evaluate the conceptual design, the mechanism has been built and equipped with sensors and actuators. Figure 8 shows a photo of the setup. Hinges h_1, h_2, and h_3 are occluded because a top plate is used to create a stiff base. Figure 1 shows the set-up without the top plate. The used material is aluminum, except for the cross-flexure hinges and linkage b_7. The latter is made out of Stavax Supreme, a high yield mold steel. The parts are discussed in more detail in Ref. [17].

6.1 Linkage b_7. As shown in Secs. 4.1 and 5.3 for the mechanism to be exactly constrained, linkage b_7 should only constrain one DOF in the axial direction. This effectively prevents the end-effector from rotating around its z-axis. This is accomplished by designing a linkage which allows one large rotation and two small rotations at each end. Kinematically, this is similar to a ball joint at each end. See Fig. 9. Both ends consist of a leaf spring with a perpendicular wire-flexure running through the center, and a notch-hinge flexure. In contrast to the hinge-flexures used at the mechanism joints, a stress release-flexure does not need a large range of motion. Therefore, the bending and torsion releases are designed to make small rotations only. However, since there are 3 DOFs at each end, the design is underconstrained. This results in an internal vibration mode, being a twist of the linkage about its longitudinal axis. However, FEM analysis shows that the natural frequency of this mode is sufficiently high and should not interfere with the dynamics at the end-effector or destabilize the controller. Hinges h_{10} and h_{11} are located directly underneath hinges h_4 and h_5, shown in Fig. 8.

6.2 Arms. As shown in Secs. 4.2, 5.4, and 5.5, the lower arms b_4, b_5, and b_6 each need to be compliant along two rotational axes for an exact constraint design. The lower arms are designed to be torsionally compliant, while being stiff in all other directions with a low mass, by having a T-shaped cross-section, shown in Fig. 10. By adding a notch flexure close to the end-effector, bending releases are implemented in the ϕ'_C-, ϕ'_D-, and φ''_E-direction, shown in Fig. 3. The arms are milled out of one aluminum block, and the notch flexure is fabricated by wire electric discharge machining (EDM).

The upper arms, b_1, b_2, and b_3, are designed as a closed box, which makes them stiff and have a low mass at the same time. The closed box consists of two halves which are bolted together. The wall thickness of the aluminum is 1 mm.

7 Measurements

An exact constraint mechanism should have a predictable behavior. We want to verify the predictability of the two-DOF stage by comparing measurements with modeling results of the actuation stiffness and the vibration mode frequencies.

We measured the actuation force by monitoring the input current through the coils. This way low frequency dynamics from cables with springs or masses and force gauges were omitted. The end-effector position was calculated using the measurements from the linear encoders. The PD-controller of the two-DOF stage was programmed to run three slow sinusoidal position reference sweeps taking three minutes in total. The cross-over frequency of the PD controller was lowered to several Hz in order to smooth the control actions. Disturbances coming from control actions of the second actuator were eliminated by switching off the second actuator and mechanically blocking its motion. Figure 11(*a*) shows the force of actuator 1, shown in Fig. 8, and the resulting x-position. The second line shows the force of actuator 2 and the resulting y-position.

The residual displacement, Fig. 11(*b*), is obtained by linear fitting, in a least square sense, the position with the force and subtracting it from the measured position. These residuals have in turn been filtered by a zero-phase first order Butterworth filter to show the trend. The measured and fitted mechanism stiffness in x-, and y-direction are, respectively, 269 N/m and 220 N/m. The stiffness according to the model with the nominal leaf-spring

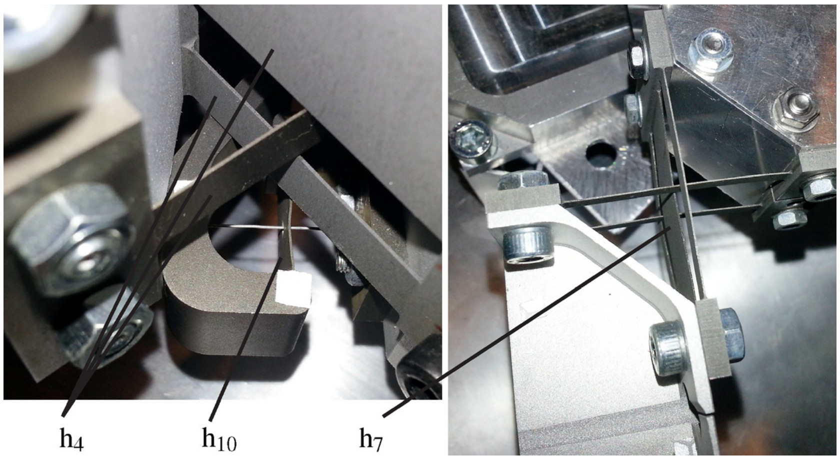

Fig. 13 Mode shape measurement setup

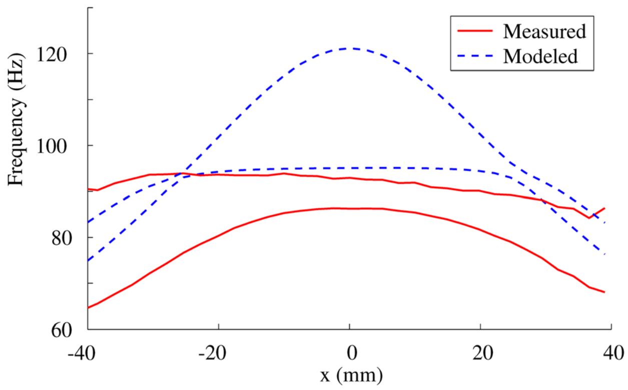

Fig. 14 Measurements of the first unwanted natural frequencies

geometry is 231 N/m and 197 N/m, which means a deviation of 15% and 10%.

The differences between model and measurements are mainly caused by tolerances on the thickness of the leaf-springs, the stiffness of the cables from the actuators and sensors, and tolerances on the alignment of the leaf-springs. We measured the thickness errors of the leaf-springs up to -9%, which should cause a decrease in actuation stiffness of up to 29%. Misalignment of leaf-springs however increases the actuation stiffness. In the neutral position of the two-DOF stage all leaf-springs of the flexures should have been flat. Because hinges h_1–h_9 consist of five leaf-springs each, they are internally overconstrained. This means not intersecting the five leaf-springs of one flexure at the instant center of rotation axis causes an increased actuation stiffness, which is a form of stiffening. We noticed that, due to tolerances on the parts, hinge h_7 showed curvature, and after a year of experimenting hinge h_{10} was somewhat skewed, Fig. 12. The combined effects of leaf-spring thickness tolerances, misalignment and parallel cable stiffness resulted in a slightly higher actuation stiffness than expected. The positional hysteresis of 1.5 mm, shown in Fig. 11(*b*), is caused by the electrical cables. The hysteresis can be minimized by using thinner cables, thinner sheathing, and proper cable routing. The repeatability with a control loop depends on the cross-over frequency of the controller, and the presence of an additional integration action. The high frequency position variations are caused by controller actions. Field strength variations of the magnets are another cause of nonlinearity. The measurements show that there is quite some hysteresis, however due to the relative smooth force to displacement characteristics, the end-effector is easily positioned within 50 nm repeatability with the controller switched on, which is the repeatability of the used linear encoder.

We measured the third and fourth natural frequency, which are the first and second unwanted frequency, of the two-DOF stage over the range of motion [37]. We used a shaker, compliantly suspended, and a laser vibrometer attached to an industrial robot to track several measurement positions. The set-up is shown in Fig. 13. We blocked actuator 2 and plotted the vibration mode frequencies against the x-displacement, shown in Fig. 14.

To verify the predictability of the dynamics the measurements are compared with the results from a multibody model, also shown in Fig. 14. While the third mode is calculated quite accurately, the fourth is less accurate. The main cause of deviation of the model from the measurements is due to alignment errors of the parts in the mechanism. Tolerances on the parts and misalignment in the assembly lead to leaf-springs not being planar in the equilibrium position. Even though this does not lead to large stress in the mechanism because of the exact constraint design, it does cause a decrease in support stiffness. For example, we ran a model of a simplified four-bar mechanism with a rotational misalignment of one of the hinges in the actuation direction of 1 deg. The results show a decrease in the vertical support stiffness at the equilibrium position of about 20% [37]. The decrease in stiffness, with respect to perfectly aligned leaf-springs, become less moving away from the equilibrium position, which is also shown by the measurements. A less significant cause of deviation of the vibration mode frequencies is the up to -9% thickness error on the leaf-springs, which leads to a 5% decrease of the third and fourth frequency.

Although the measured actuation stiffness and third and fourth vibration mode frequency deviate considerably from the modeled values, it is much less than the decrease in stiffness which would appear due to bifurcation. In the case of Meijaard et al. [21], a small rotational misalignment of 6 mrad led to bifurcation and a reduction of actuation and supporting stiffness of roughly one decade. This stiffness reduction is much more than we measured, and it appeared more sudden. The two actuation stiffnesses and the third and fourth vibration mode frequencies are predicable. Even with significant misalignments load stiffening is minimized, and bifurcation is prevented. We conclude that designing an assembled mechanism in an exactly constrained manner leads to predictable stiffnesses and modal frequencies.

8 Conclusions

We presented the exact constraint analysis and design of a two degrees of freedom cross-flexure-based stage. To ensure a deterministic behavior with the many specifically designed and assembled parts the design was made exactly constrained. Three methods were used to analyze the constraints of the mechanism. The method using Grüblers criterion requires background knowledge on either the number of overconstraints or the mobility to calculate the mobility or the number of overconstraints, respectively. Therefore, the criterion on its own cannot be used to identify the constraints of a mechanism if overconstraints are present. The method of opening the kinematic loop and analyzing the constraints meeting from the two sides shows possible under- and overconstraints, and their direction. The method provides good insight but the analysis can be difficult in particular with 3D mechanisms. Grüblers criterion can serve as a check on the number of constraints and the mobility. The mathematical method using the multibody model with singular value decomposition undoubtedly determines the amount of overconstraints companied with their indeterminate stress modes, and the mobility with the accompanying motions.

The two degrees of freedom mechanism consists of three kinematic loops. With ideal rigid bodies and single degree of freedom hinges each kinematic loop gives rise to three overconstraints adding to the total of nine overconstraints in the mechanism. To obtain an exact constraint mechanism we implemented nine releases in the fabricated set-up.

The measured actuation stiffness and third and fourth vibration mode frequency are quite close to the modeled values. Due to the exact constrained design there is no bifurcation, and load stiffening is minimized, even though there are various errors causing nonlinearity. The main cause of deviation in the support stiffness is misalignment of the assembly which leads to leaf-springs not being planar in the equilibrium position. Although this does not lead to large stress in the mechanism because of the exact constraint design, it can cause a considerable decrease in support stiffness. We conclude that designing an assembled mechanism in an exactly constrained manner leads to predictable stiffnesses and modal frequencies.

Acknowledgment

The authors like to thank L. Tiemersma for the help during the production and assembly of the mechanism, F. Hoitzing, H. M. J. R. Soemers, and J. L. Herder for the concept generation that formed the basis of this work, and W. Wijma for the laservibrometer measurements. This research was supported by the Dutch association Point-One, project MOV-ET PNE08006, from the Dutch Ministry of Economic Affairs.

References

[1] Eastman, F. S., 1935, "Flexure Pivots to Replace Knife Edges and Ball Bearings," Engineering Experiment Station Bulletin 86, University of Washington.
[2] Hale, L. C., 1999, "Principles and Techniques for Designing Precision Machines," Ph. D. thesis, University of California, Livermore, CA.
[3] Soemers, H. M. J. R., 2010, *Design Principles for Precision Mechanisms*, T-Pointprint, Enschede.
[4] Haringx, J. A., 1949, "The Cross-Spring Pivot as a Constructional Element," Appl. Sci. Res., Sect. A, **1**(1), pp. 313–332.
[5] Jones, R. V., 1956, "A Parallel-Spring Cross-Movement for an Optical Bench," J. Sci. Instrum., **33**(7), pp. 279–280.
[6] Paros, J. M., and Weisbord, L., 1965, "How to Design Flexure Hinges," Mach. Des., **37**(25), pp. 151–156.
[7] Eijk, J. V., 1985, "On the Design of Plate Spring Mechanism," Ph.D. thesis, Delft University of Technology, Delft, The Netherlands.
[8] Jones, R. V., 1988, *Instruments and Experiences, Papers on Measurement and Instrument Design*, Wiley, New York.
[9] Smith, S. T., 2000, *Flexures: Elements of Elastic Mechanisms*, Taylor & Francis, London, England.
[10] Howell, L. L., 2001, *Compliant Mechanisms*, Wiley, New York.
[11] Zelenika, S., and de Bona, F., 2002, "Analytical and Experimental Characterisation of High-Precision Flexural Pivots Subjected to Lateral Loads," Precis. Eng., **26**(4), pp. 381–388.
[12] Henein, S., Spanoudakis, P., Droz, S., Myklebust, L. I., and Onillon, E., 2003, "Flexure Pivot for Aerospace Mechanisms," Proceedings of the 10th ESMATS/ESA, Vol. 10, pp. 285–288.
[13] Awtar, S., and Slocum, A. H., 2007, "Constraint-Based Design of Parallel Kinematic XY Flexure Mechanisms," ASME J. Mech. Des., **129**(8), pp. 816–830.
[14] Hopkins, J. B., and Culpepper, M. L., 2010, "Synthesis of Multi-Degree of Freedom, Parallel Flexure System Concepts Via Freedom and Constraint Topology (FACT)—Part I: Principles," Precis. Eng., **34**(4), pp. 259–270.
[15] Brouwer, D. M., Meijaard, J. P., and Jonker, J. B., 2013, "Large Deflection Stiffness Analysis of Parallel Prismatic Leaf-Spring Flexures," Precis. Eng., **37**(3), pp. 505–521.
[16] Wiersma, D. H., Boer, S. E., Aarts, R. G. K. M., and Brouwer, D. M., 2012, "Large Stroke Performance Optimization of Spatial Flexure Hinges," Proceedings of the 1st Biennial International Conference on Dynamics for Design, No. DETC2012-70502.
[17] Folkersma, K. G. P., Boer, S. E., Brouwer, D. M., Herder, J. L., and Soemers, H. M. J. R., 2012, "A 2-DOF Large Stroke Flexure-Based Positioning Mechanism," Proceedings of the 36th Mechanisms and Robotics Conference, No. DETC2012-70377.
[18] Blanding, D., 1999, *Exact Constraint Machine Design Using Kinematic Principles*, ASME Press, New York.
[19] Brouwer, D. M., Boer, S. E., Meijaard, J. P., and Aarts, R. G. K. M., 2013, "Optimization of Release Locations for Small Stress Large Stiffness Flexure Mechanisms," Mech. Mach. Theory, **64**, pp. 230–250.
[20] Awtar, S., Shimotsu, K., and Sen, S., 2010, "Elastic Averaging in Flexure Mechanisms: A Three-Beam Parallelogram Flexure Case Study," ASME J. Mech. Rob., **2**(4), p. 041006.
[21] Meijaard, J. P., Brouwer, D. M., and Jonker, J. B., 2010, "Analytical and Experimental Investigation of a Parallel Leaf Spring Guidance," Multibody Syst. Dyn., **23**, pp. 77–97.
[22] Maxwell, J. C., 1864, "On the Calculation of the Equilibrium and Stiffness of Frames," Philos. Mag., **27**(4), pp. 294–299.
[23] Chebychev, P. L., 1907, *Sur les parallélogrammes*, Oeuvres, Tome II, pp. 85–106.
[24] Grübler, M., 1883, "Allgemeine Eigenschaften der Zwangläufigen ebenen kinematischen Ketten," Civilingenieur, **29**, pp. 167–200.
[25] Kutzbach, K., 1929, "Mechanische Leitungsverzweigung, ihre Gesetze und Anwendungen," Maschinenbau. Betrieb, **8**, pp. 710–716.
[26] Besseling, J. F., 1979, "Trends in Solid Mechanics 1979," Proceedings of the Symposium Dedicated to the 65th Birthday," W. T. Koiter, J. Besseling, and A. van der Heijden, eds., Delft University Press, pp. 53–78.
[27] Pellegrino, S., and Calladine, C. R., 1986, "Matrix Analysis of Statically and Kinematically Indeterminate Frameworks," Int. J. Solids Struct., **22**(4), pp. 409–428.
[28] Angeles, J., and Gosselin, C., 1989, "Détermination du degré de liberté des chaînes cinématiques," Transactions de la Société Canadienne de Génie Mécanique, **12**, pp. 219–226.
[29] Aarts, R. G. K. M., Meijaard, J. P., and Jonker, J. B., 2012, "Flexible Multibody Modelling for Exact Constraint Mechatronic Design of Compliant Mechanisms," Multibody Syst. Dyn., **27**(1), pp. 119–133.
[30] Nelder, J. A., and Mead, R., 1965, "A Simplex Method for Function Minimization," Comput. J., **7**(4), pp. 308–313.
[31] Ryu, J. W., Gweon, D.-G., and Moon, K. S., 1997, "Optimal Design of a Flexure Hinge Based XY Wafer Stage," Precis. Eng., **21**(1), pp. 18–28.
[32] Culpepper, M. L., and Anderson, G., 2004, "Design of a Low-Cost Nano-Manipulator Which Utilizes a Monolithic, Spatial Compliant Mechanism," Precis. Eng., **28**(4), pp. 469–482.
[33] Yao, Q., Dong, J., and Ferreira, P. M., 2007, "Design, Analysis, Fabrication, and Testing of a Parallel-Kinematic Micropositioning XY Stage," Int. J. Mach. Tools Manuf., **47**(6), pp. 946–961.
[34] de Jong, B. R., Brouwer, D. M., de Boer, M. J., Jansen, H. V., Soemers, H. M. J. R., and Krijnen, G. J. M., 2010, "Design and Fabrication of a Planar Three-DOFs MEMS-Based Manipulator," J. Microelectromech. Syst., **19**(5), pp. 1116–1130.
[35] Werner, C., Rosielle, P. C. J. N., and Steinbuch, M., 2010, "Design of a Long Stroke Translation Stage for AFM," Int. J. Mach. Tools Manuf., **50**(2), pp. 183–190.
[36] Boer, S. E., Aarts, R. G. K. M., Brouwer, D. M., and Jonker, J. B., 2010, "Multibody Modelling and Optimization of a Curved Hinge Flexure," The 1st Joint International Conference on Multibody System Dynamics, Lappeenranta, pp. 1–10.
[37] Wijma, W., Boer, S. E., Aarts, R. G. K. M., Brouwer, D. M., and Hakvoort, W. B. J., 2013, "Modal Measurements and Model Corrections of a Large Stroke Compliant Mechanism," ECCOMAS Multibody Dynamics 2013, July 1–4, 2013, University of Zagreb, Croatia, pp. 831–843.